Multibeam Echosounder With Orthogonal Waveforms: Feasibility and Potential Benefits

Antoine Blachet, Andreas Austeng, *Senior Member, IEEE*, Joaquín Aparicio, *Member, IEEE*, Alan J. Hunter, *Senior Member, IEEE*, and Roy Edgar Hansen, *Senior Member, IEEE*

***Abstract*—Modern multibeam echosounders (MBE) employ frequency-division techniques (FDT) to ensonify multiple sectors within the same ping cycle. This leads to improved performance in coverage rate, and yaw and pitch stabilization. However, it introduces a bias among sectors because MBES systems are frequency dependent. It also reduces the maximum pulse bandwidth compared to a single-sector sonar. In this study, we consider the code-division technique (CDT) as a solution to this problem. A set of orthogonal coded pulses are received within the same frequency band, and each sector is separated with a matched filter. We assess the feasibility of the technique through two stages. 1) First, we formulate an analytical model describing the power and crosstalk budgets of any multisector MBES. The model can then be used to design transmission sequences fitting these budgets. 2) Then, we display the practical usage of the technique for MBES imaging and mapping through simulated case studies. For the same total time-bandwidth budget, we compare the performance of FDT, CDT, and multicarrier CDT (MC-CDT), a hybrid method employing CDT and FDT, which is robust to strong dynamic backscatter. This study considers only bottom detection based on signal amplitude. Our results show that it is possible to share a larger frequency bandwidth between multiple sectors while maintaining an acceptable bottom detection performance similar to FDT. Our choice of time-bandwidth product with CDT offers a crosstalk suppression of −25 dB between sectors, but may display low-magnitude residual artefacts in the water-column data. MC-CDT provides a significant gain of pulse bandwidth while it offers interband separation performance comparable to FDT and reduces significantly the water-column artefacts.**

***Index Terms*—Modulated signals, multibeam echosounder (MBES), orthogonal waveforms, seafloor bathymetry, sonar signal processing.**

I. Introduction

MULTIBEAM echosounders (MBES) are one of the most effective tools for mapping and resolving seabed morphology [1], [2]. The technology has evolved from narrowband single swath sonars [3] (1977) to broadband multiple subsector imaging systems [2], [4], [5], as illustrated in Fig. 1. In multisector MBES, the transmit beam is broken down into sectors that can be independently focused within a single ping cycle. This leads to increased performance. Multiple along-track sectors (or multiswath) enhance the density of soundings of a single ping, which results in improved coverage rate [2]. Multiple across-track sectors enable active yaw and pitch stabilization, which ensures that perturbations of the vessel no longer result in gaps in seafloor coverage [2]. Finally, independent transmissions allow the separation of noise from sidelobes by adjusting the source level per sector.

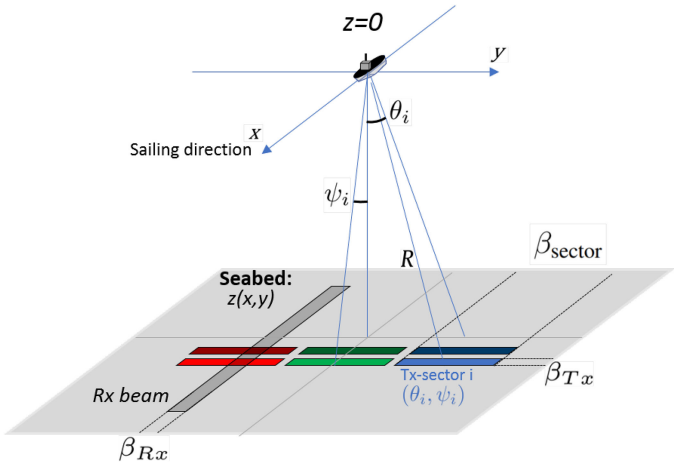

Fig. 1. Illustration of a multisector MBES (three sectors, two swaths). The beam footprints of the transmitted sectors are visible in different colors. The Tx array of resolution β_{Tx} along-track and β_{sector} across-track is located along the x-axis. The orthogonal Rx-array of resolution β_{Rx} is located along the y-axis.

Today's systems achieve sector separation through allocating different frequency bands to each sector. The same principle is also successfully used by some advanced fishery research MBES [6]. However, frequency-division techniques (FDT) have three main drawbacks. 1) The backscatter (BS), the water-column environment, and the array beam patterns are frequency dependent [1], [4]. This limits the potential of sediment acoustic characterization [4], [7]. 2) Moreover, it requires radiometric corrections [8] and absorption compensation per sector, which are sources of error [4], [7]. 3) The last disadvantage is the nonoptimal use of the bandwidth, a limited resource for active sonars [9]. A significant part of the bandwidth must be allocated to frequency guard bands [10] that do not contain any

Manuscript received March 2, 2020; revised November 6, 2020 and December 16, 2020; accepted December 31, 2020. Date of publication April 15, 2021; date of current version July 14, 2021. This work was supported in part by the Center for Innovative Ultrasound Solutions and in part by the Research Council of Norway under Grant 237887. *(Corresponding author: Antoine Blachet.)*

Associate Editor: M. Hayes.

Antoine Blachet, Andreas Austeng, and Joaquín Aparicio are with the Digital Signal Processing and Image Analysis Group, Department of Informatics, University of Oslo, 0316 Oslo, Norway (e-mail: antoine.blac@gmail.com; Andreas.Austeng@ifi.uio.no; joaqapar@ifi.uio.no).

Alan J. Hunter is with the University of Bath, Bath BA2 7AY, U.K., and also with the University of Olso, 0316 Oslo, Norway (e-mail: ajh210@bath.ac.uk).

Roy Edgar Hansen is with the Norwegian Defence Research Establishment (FFI), N-2027 Kjeller, Norway, and also with the University of Olso, 0316 Oslo, Norway (e-mail: Roy-Edgar.Hansen@ffi.no).

Digital Object Identifier 10.1109/JOE.2021.3052568

information, limiting the maximum bandwidth per sector for the multisector mode compared to the single sector [11], [12].

Orthogonal waveform modulation techniques provide a solution for separating signals overlapping in frequency and time. Originally developed for GPS localization and wireless communication [13], they form the basis of the code-division technique (CDT). This strategy permits the sharing of the same wide frequency band between users. Today, CDT is also used in Radar [14]–[21] and Sonar [22], [23] and has been successfully tested in seismic reflection imaging [24]–[28], synthetic aperture radar [29], ultrasound localization [30], and investigated for medical ultrasound applications [31]–[39].

In this article, we study the feasibility of orthogonal waveforms for a multisector MBES system with amplitude detection. We show that allocating the same frequency band for all sectors while maintaining bottom detection performance is possible. However, residuals of the matched filter generate noise that might not be suitable for all mapping scenarios. Depending on the dynamic range of the seabed backscatter, we consider a hybrid method combining frequency and code division. This provides a significant gain of bandwidth and reduces the difference of central frequency between sectors. We test and validate the different strategies on simulated MBES channel data.

This study is organized as follows. In Section II, we present the theory on multisector MBES and describe the CL as a function of system configuration and seabed properties. In Sections III and IV, we present the requirements on waveform orthogonality and, then, review three modulation techniques suited for different bandwidth allocation strategies. We describe the simulated case study and present the results in Sections V and VI. Section VII gathers a discussion about the results, and Section VIII outlines the main conclusions of this work. Table I summarizes the main abbreviations.

TABLE I
TABLE OF MAIN ABBREVIATIONS

Abbreviation	
BL_i	backscatter level
$BP_{R/T}$	beam pattern (receive/transmit)
BPSK-PRN	binary phase shift keying - pseudo random noise
BS	seafloor backscatter
CDT	code division technique
CL	cross-talk level
DFCW	discrete frequency coded waveform
FDT	frequency division technique
LFM	linear frequency modulation
MBES	multibeam echo sounder
MC-CDT	multi carrier - code division technique
NL	noise level
OLFM	orthogonal linear frequency modulation
PASR	peak-to-auto-correlation-sidelobe ratio
PCCR	peak-to-cross-correlation ratio
PG	pulse compression gain
SCR	signal-to-cross-talk ratio
SL_i	source level
TBP	time-bandwidth product
TL_i	transmission loss
TS_i	target strength
RT	reception threshold
SNR	signal-to-noise ratio

II. Multisector Transmissions

A. Principle

The principles of multisector MBES transmission and processing are illustrated in Figs. 1 and 2. The sonar operates by transmitting a set of N different signals, s_i, within the same ping cycle. Each transmission sector is emitted at a time t_i and focused in the acros-track (θ_i) and along-track (ψ_i) directions.

The signal processing follows the conventional MBES routine described in [1]. After compensating for the transmission delays t_i, each sector is processed and beamformed individually in its own angular window. Multiple sector images are combined to reconstruct the full swath water-column data. Conventional MBES employs bandpass filters to separate the different frequency bands Δf_i. An MBES based on orthogonal waveforms relies on a matched filter, where the low cross-correlation between signals within the same frequency band enables crosstalk suppression.

B. Multisector Power Equation

The level of crosstalk generated by a given sonar system can be derived from the standard sonar equation for an extended target [40]. Before processing, the backscatter level (BL) BL_i, in dB, of a sector i steered in the direction (θ_i, ψ_i) and received in the direction θ is [4]

$$BL_i(\theta, \psi_i) = SL_i + BP_T(\theta_i, \psi_i) - 2TL_i + BS_f(\theta) + TS \quad (1)$$

where SL_i is the source level in sector i. In the case of N simultaneous transmissions, the source level of each transmission can be considered as $1/N$ of the maximum source level.

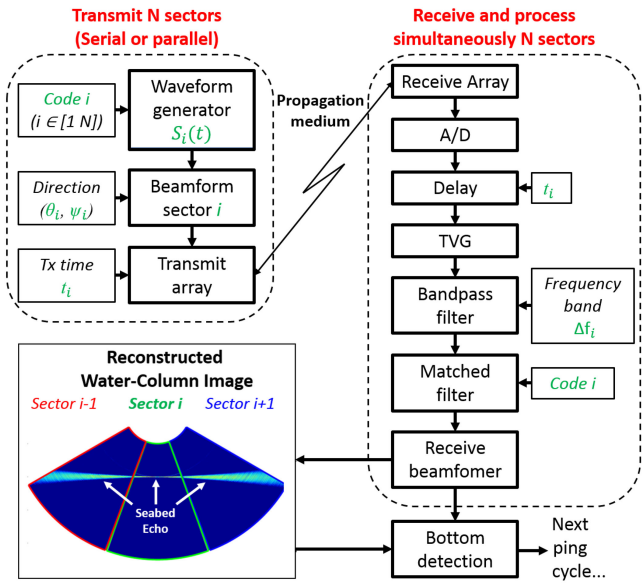

Fig. 2. Block diagram of a multisector MBES. N sectors are transmitted and processed independently, and the full swath water-column data are reconstructed after beamforming.

Note that in the case of sequential transmissions, the source level can be maximum at each transmission. $\mathrm{BP}_T(\theta_i, \phi_i)$ is the emission beam pattern of sector i. TL_i are the transmission losses associated with sector i. The target strength is defined as: $\mathrm{TS} = \mathrm{BS}_f(\theta) + 10\log_{10}(A/A_{\mathrm{ref}})$, where the seafloor BS is $\mathrm{BS}_f(\theta)$, A is the acoustic footprint area and A_{ref} the reference area (see [1, p. 108] for detailed explanations). For a flat seafloor, the footprint area A can take two different forms, depending on whether the spatial extent of the resolution cell located at range R is limited by the beam resolution ($\beta_{Rx/Tx}$) or by the pulse length after matched-filtering ΔR [41, pp. 48–49]

$$A = \begin{cases} \dfrac{R\beta_{Tx}\Delta R}{\sin(\theta)\cos(\phi_i)}, & \text{Pulse-limited} \\ \dfrac{R\beta_{Tx}R\beta_{Rx}}{\cos(\theta)\cos(\phi_i)}, & \text{Beam-limited.} \end{cases} \tag{2}$$

After beamforming at the receiver and matched filtering, bottom detection is possible if the signal level is above the threshold RT, in dB,

$$\mathrm{BL}_i(\theta, \psi_i) + \mathrm{BP}_R(\theta) + \mathrm{PG} - \mathrm{NL} - \mathrm{CL} > \mathrm{RT} \tag{3}$$

where $\mathrm{BP}_R(\theta)$ is the reception beam pattern. CL is the crosstalk level, which is a multiplicative source of noise (proportional to the source level). The additive noise level is $\mathrm{NL} = N_0\Delta f_i$, where N_0 is the noise density, assumed constant over the bandwidth Δf_i. $\mathrm{PG} = 10\log_{10}(BT_P)$ is the pulse compression gain defined as the product of the pulse length T_p and pulse bandwidth B. It must be noted that the advantage provided by pulse compression is only optimum in the beam-limited regime. In the pulse-limited regime, increasing the bandwidth with fixed pulse length will decrease the target strength by reducing the size of the footprint A in (2). Increasing pulse length with fixed bandwidth increases signal-to-noise ratio (SNR) in all cases.

C. Nature of the Crosstalk

The term CL in (3) corresponds to the multiplicative noise from the $(N-1)$ other sectors interfering with sector i such as

$$\mathrm{CL} = 10\log_{10}\left(\sum_{j\neq i} 10^{(\mathrm{BL}_j(\theta_j,\psi_j)+\mathrm{CC}_{ij})/10}\right) \tag{4}$$

where $\mathrm{CC}_{ij} = 10\log_{10}(\mathrm{CC})$, with CC, the evaluated cross-correlation function between the two waveforms.

The amount of multiplicative noise is measured by the signal-to-crosstalk ratio (SCR), defined before ($\mathrm{SCR}_{\mathrm{in}}$) or after ($\mathrm{SCR}_{\mathrm{out}}$) matched filtering as

$$\begin{aligned} \mathrm{SCR}_{\mathrm{out}} &= \mathrm{BL}_i(\theta, \psi_i) + \mathrm{BP}_R(\theta) + \mathrm{PG} - \mathrm{CL} \\ &= \mathrm{SCR}_{\mathrm{in}} + \mathrm{PG} - \mathrm{CC}_{ij}. \end{aligned} \tag{5}$$

The SCR is a function of both the sonar configuration and the seabed characteristics. Depending on the relationship between sectors, the crosstalk CL_j can take different forms. We consider four different types, illustrated in Fig. 3. Then, we evaluate in Table II, the value of $\mathrm{SCR}_{\mathrm{in}}$ for each contribution with a generic sonar configuration ($\mathrm{BP}_R(\theta) = \mathrm{BP}_T(\theta) = +30$ dB, $R \in$ [100–200] m and $\mathrm{BS}_f \in [-10\ \ -30]$ dB).

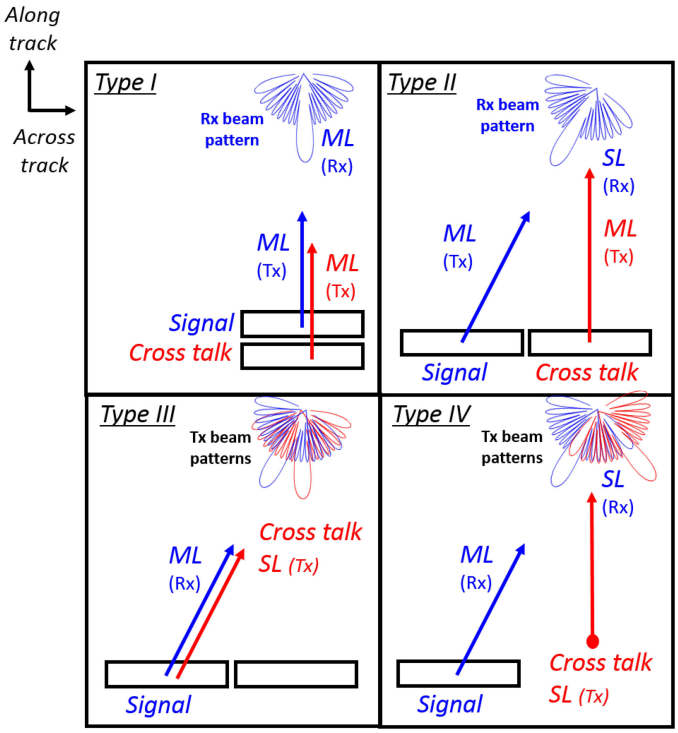

Fig. 3. Illustration of the four types of crosstalk between sectors. Each case corresponds to a specific permutation of transmit and receive sidelobe (SL) and mainlobe (ML).

TABLE II
EXAMPLE OF THEORETICAL SCRS BEFORE MATCHED FILTERING

$\mathrm{SCR}_{\mathrm{in}}$	Type I	Type II	Type III	Type IV
Magnitude [dB]	0	[-50 to 0]	-30	under -60

1) Type I: Mainlobe (Tx)–Mainlobe (Rx): When two sectors are steered in the same across-track direction, both signals will travel through a similar acoustic path ($\mathrm{BS}(\theta_i) = \mathrm{BS}(\theta_j)$ and $\mathrm{TL}_i = \mathrm{TL}_j$). They will be backscattered at a similar level and angular direction. Receive beamforming will not separate the two signals. This occurs mostly between different swaths and at the transitions between sectors. In this case, the SCR is only determined by the cross-correlation properties

$$\mathrm{SCR}_{\mathrm{out}} = \mathrm{PG} - \mathrm{CC}_{ij}. \tag{6}$$

2) Type II: Mainlobe (Tx)–Sidelobe (Rx): When the transmit mainlobe of another sector is received simultaneously with the signal, then

$$\begin{aligned} \mathrm{SCR}_{\mathrm{out}} = (\mathrm{PG} - \mathrm{CC}_{ij}) + \mathrm{BP}_R(\theta, \psi_i) \\ + \mathrm{BS}(\theta_i) - \mathrm{BS}(\theta_j) - 2(\mathrm{TL}_i - \mathrm{TL}_j). \end{aligned} \tag{7}$$

The SCR now contains the contrast of backscatter $\mathrm{BS}(\theta_i) - \mathrm{BS}(\theta_j)$, which might be significant in the case of specular reflection. We note that reducing the source level of the sector mitigates this effect but reduces the SCR of type I at the sector boundaries.

3) Type III: Sidelobe (Tx)–Mainlobe (Rx): A transmit sidelobe from a sector steered in another across-track direction will travel again through a similar acoustic path; then, the SCR will be

$$\mathrm{SCR_{out}} = \mathrm{PG} - \mathrm{CC}_{ij} + \mathrm{BP}_T(\theta, \psi_i). \tag{8}$$

4) Type IV: Sidelobe (Tx)–Sidelobe (Rx): Finally, the contribution from all scatterers located outside of the transmit sector mainlobes is

$$\begin{aligned}\mathrm{SCR_{out}} = \mathrm{PG} - \mathrm{CC}_{ij} + \mathrm{BP}_T(\theta_i, \psi_i) + \mathrm{BP}_R(\theta, \psi_i) \\ - 2(\mathrm{TL}_i - \mathrm{TL}_j) + (\mathrm{BS}(\theta_i) - \mathrm{BS}(\theta_j)).\end{aligned} \tag{9}$$

D. Delay Considerations for Sector Transmission

Multisector transmissions confer the possibility to emit each sector independently. In this context, it is relevant to optimize the order in which the pulses are transmitted. Considering $\Delta t_{\text{spread-max}}$ as the largest time window occupied by a beam in the echogram data; then, two sectors i and j steered in the same across-track direction will be separated if transmitted with a delay

$$|t_i - t_j| > \Delta t_{\text{spread-max}} + T_p. \tag{10}$$

For a flat seafloor at depth H, this delay can be expressed as

$$\Delta t_{\text{spread-max}} = \frac{H}{c}\left(\cos\left(\theta - \frac{\beta_{Rx}}{2}\right) - \cos\left(\theta + \frac{\beta_{Rx}}{2}\right)\right). \tag{11}$$

Consequently, it is possible to avoid crosstalk of Type I by designing transmission sequences that follow the condition given by (10) between sectors located in the same across-track direction. This strategy is also expected to perform better for central sectors as $\Delta t_{\text{spread-max}}$ will be smaller. However, it requires *a priori* knowledge of the bathymetry, which can be derived from the previous pings in many cases. This problem will not be addressed in this study.

III. Orthogonal Waveforms

In this section, we select waveforms with desired autocorrelation and cross-correlation properties. First, we introduce some metrics that quantify the orthogonality; then, we review potential candidates.

A. Background on Orthogonal Signals

Two signals $s_i(t)$ and $s_j(t)$ received with a delay τ and processed by a matched filter are orthogonal when their cross correlation in the time or frequency domain is zero

$$s_i \star s_j(\tau) = \begin{cases} \int_{-\infty}^{+\infty} s_i(t) s_j(t+\tau) dt = 0 \\ \mathcal{F}^{-1}[S_i^*(f) S_j(f)] = 0 \end{cases} \tag{12}$$

where $\mathcal{F}^{-1}$ denotes the inverse Fourier transform, $S_i(f)$ and $S_j(f)$ are the Fourier transforms of $s_i(t)$ and $s_j(t)$, respectively, and $*$ denotes the complex conjugate. We see that perfect orthogonality is not possible without exclusive spectral support for all time shifts τ. Moreover, signals of finite length occupying different frequency bands will exhibit spectral sidelobes that also prevent perfect orthogonality. In this context, a residual crosstalk signal will always remain after matched filtering, both with code or frequency division.

Because it is critical to ensure that the autocorrelation and cross-correlation properties remains suitable for imaging, we consider two metrics: 1) the peak-to-autocorrelation-sidelobe ratio (PASR) and 2) the peak-to-cross-correlation ratio (PCCR) [42], [43]

$$\mathrm{PASR}(i) = 10\log_{10}\left(\max\left(\mathrm{abs}\left(\frac{s_i \star s_i(\tau)}{s_i \star s_i(0)}\right)\right)\right) \tag{13}$$

$$\mathrm{PCCR}(i,j) = 10\log_{10}\left(\max\left(\mathrm{abs}\left(\frac{s_i \star s_j(\tau)}{s_i \star s_i(0)}\right)\right)\right). \tag{14}$$

The PASR controls the peak sidelobe values of the AC. It has to be as low as possible since sidelobes can mask an object in the water-column, trigger false detection and are known to affect the accuracy of bottom detection algorithms [44]. The PCCR provides the highest bound of the cross-correlation function and must be used when evaluating the CL term in (3). These two metrics allow us to assess the robustness of the system in terms of accuracy and false detection as they represent the worst case values of auto and cross-correlation functions. Other metrics such as the peak-to-integrated-sidelobe ratio and the peak-to-integrated-cross-correlation ratio [42] may complement the waveforms selection.

B. Modulation Schemes

Considering the general expression of a complex signal $s(t)$ of constant envelope A

$$s(t) = Ae^{j(\omega(t)t + \theta(t))} \tag{15}$$

orthogonal waveforms are constructed by modulating either the frequency $\omega(t)$ or the phase $\theta(t)$ of each signal with pairs of orthogonal sequences. The literature on waveform design is extensive [13], [15], [16] and a significant number of potential candidates can be named. We present and compare three modulation techniques with complementary properties: linear frequency modulation (LFM), pseudorandom noise binary phase modulation, and discrete frequency hopping. In the selected examples, pulse length, bandwidth, time-bandwidth product (TBP), and the carrier frequency f_0 of the waveforms are comparable.

1) Orthogonal LFM: Two pulses with low cross-correlation function can be obtained by sweeping LFM signals with opposite slope (see Fig. 4). The major advantage of the LFM waveform is its almost flat spectrum obtained by spending the same time (and energy) at all frequencies. It is an efficient way of using the bandwidth (high spectral efficiency) [15]. It makes the orthogonal LFM (OLFM) an excellent candidate for FDT, and multicarrier CDT (MC-CDT).

The PASR value is high: about -13.3 dB [43], which requires amplitude weighting. A pair of up–down chirps has the best orthogonal properties among all other waveforms, with a PCCR approximated to $1/(BT_p)^{1/2}$ [17], [42]. The main disadvantage of OLFM is that only one pair exists for an assigned value of bandwidth.

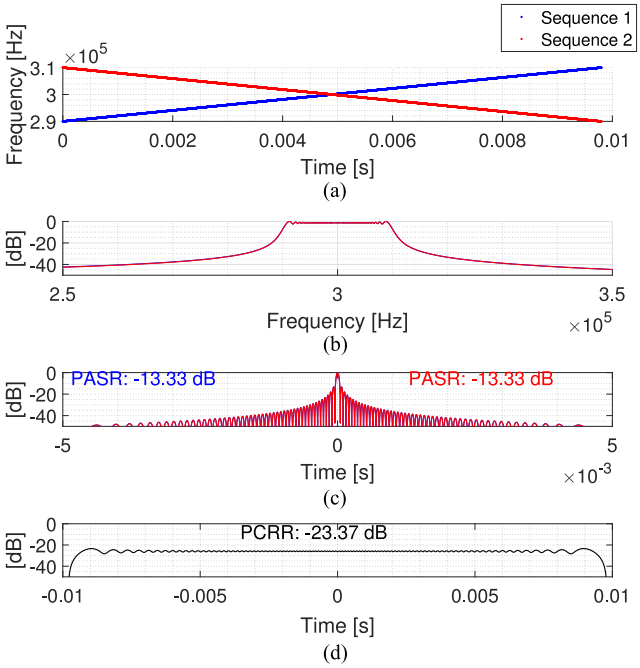

Fig. 4. Example of two orthogonal LFM sequences. (a) Modulation sequences. (b) Amplitude spectra. (c) Autocorrelation functions. (d) Cross-correlation function. $f_0 = 300$ kHz, $T_p = 12.75$ ms, TBP $= 255$.

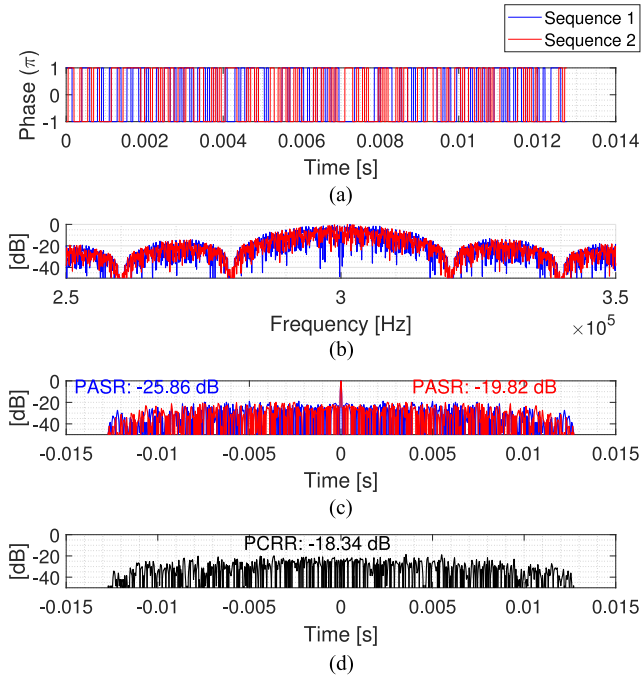

Fig. 5. Example of two BPSK-PRN sequences. (a) Modulation sequences. (b) Amplitude spectra. (c) Autocorrelation functions. (d) Cross-correlation function. $f_0 = 300$ kHz, $T_p = 12.75$ ms, $M = 255$, TBP $= 255$.

2) Modulation of Orthogonal Sequences by Binary Phase-Shift Keying: Binary phase-shift keying pseudorandom noise (BPSK-PRN) modulation is a CDT known for generating a large number of orthogonal signals. The phase of a continuous wave (CW) pulse is modulated with a binary sequence of length M

$$\theta(t) = \{\theta_1, \theta_2, \ldots, \theta_M\}, \qquad \text{with } \theta_i = \pm\pi. \tag{16}$$

The preferred candidates for BPSK-PRN sequences are Kasami and Gold sequences of length $M = 2^n - 1$ (where n is an integer), as they provide the theoretical best auto and cross-correlation properties for large sets of codes [45], [46].

A pair of Kasami BPSK-PRN signals is showed in Fig. 5. The frequency spectrum is no longer rectangular but is defined by $f \longmapsto \text{sinc}((f - f_0)\pi M/T_p)$, which has significant sidelobes. In practice, we observe that bandpass filtering beyond the first null does not significantly affect the autocorrelation and cross-correlation properties. However, the energy content outside of the -3 dB bandwidth is still significant compared to the other waveforms. It makes this waveform less suited for FDT and MC-CDT. The autocorrelation function has a temporal resolution of about T_p/M. The main drawback of this waveform is its sidelobes with an aspect of colored random noise. The sidelobe level is relatively low but does not decrease with time. Contrary to LFM, tapering BPSK-PRN pulses does not reduce the sidelobes significantly. A solution for reducing the PASR consists in employing waveforms with large TBP. Under this condition, the sidelobe-induced noise approaches the effect of low-power additive white Gaussian noise and does not limit the bottom detection accuracy. The properties of the cross correlation vary between pairs of sequences, but the PCCR is theoretically bounded by: $(1 + 2^{n/2+1})^2/M^2$ [42]. Also, we have observed that the average value of a sequence approaches: $2/(BT_p)^{1/2}$. This waveform is a good candidate for sharing the system's full bandwidth between all sectors (CDT). As the number of codes in the set is relatively limited, finding a subset with good cross-correlation properties with numerical optimization techniques is advised. In this article, we have used a set of Kasami codes, which showed the lowest cross-correlation values.

3) Discrete Frequency-Coding Waveform With Frequency Hopping: Discrete frequency-coding waveform with frequency hopping (i.e., DFCW) is another CDT known for generating orthogonal signals. It consists of a train of short subpulses where the carrier frequency f_m changes randomly from subpulse to subpulse according to a sequence of M different integers $a_m \in [\![1; M]\!]$

$$f_m = f_0 + \frac{a_m}{t_b} \tag{17}$$

where $t_b = T_p/M$ is the length of a subpulse.

The Costas matrix provides sets of sequences with excellent properties [17], [47]. In this article, we used a database of Costas arrays [48].

Example of Costas DFCW waveforms are showed in Fig. 6. The advantage of DFCW compared to BPSK-PRN is the relatively flat spectrum obtained by spending the same time on each subpulse. The waveform was designed to have a continuous phase and the spectrum has a bandwidth defined by $B = M^2/T_p$ and low sidelobes. We observe that the lower bound of the PCCR approaches also $2/(BT_p)^{1/2}$. These properties makes DFCW a good waveform for MC-CDT, where more than two sectors

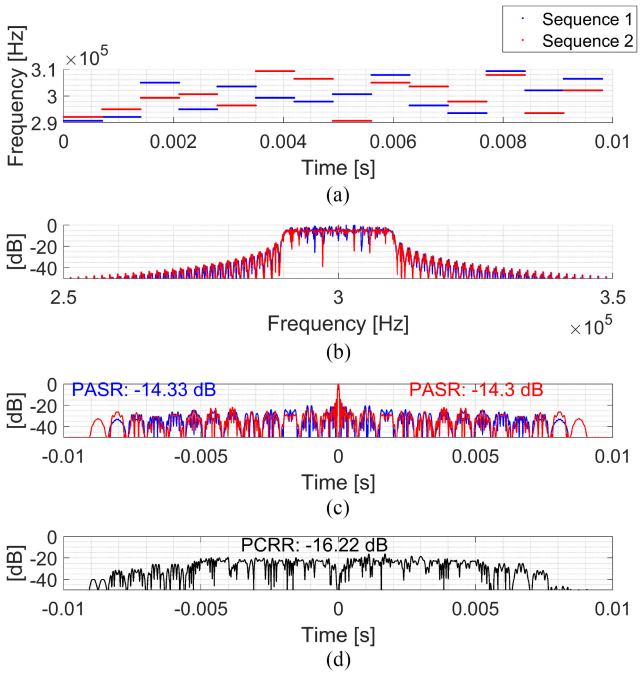

Fig. 6. Example of two Costas coded sequences. (a) Modulation sequences. (b) Amplitude spectra. (c) Autocorrelation functions. (d) Cross-correlation function. $f_0 = 300$ kHz, $T_p = 9.8$ ms, $M = 14$, TBP $= 196$.

can coexist. However, for $M < 23$, a large number of codes exist, and finding the best subset requires the use of advanced numerical optimization techniques. In practice, it is more difficult to find codes reaching the PCCR values obtained with the previous BPSK-PRN design [17]. On the other hand, only a few codes exist beyond the order 25 [15]. The autocorrelation has a resolution of T_p/M^2 and nonuniform sidelobes comparable to the BPSK-PRN waveform. Other types of modulation, such as LFM [49] and phase modulation [50] may be added to Costas signals to improve some properties such as the sidelobe level without increasing the order of the code. However, no significant benefit has been reported regarding orthogonality.

4) Comparison of Performance: Fig. 7 compares the PCCR of the three simulated waveforms for a varying TBP. Using up–down chirps (OLFM) in Fig. 7 provides the best orthogonal properties. BPSK-PRN requires large TBPs but permits the achievement of cross correlation in the range of -20 dB to -25 dB. This range of values can satisfy the bottom detection requirements presented in Table II, but is inferior to the performance of FDT where the common spectral support between two bands after bandpass filtering can be extremely low (-20 dB to -100 dB). Finally, DCFW offers PCCR values slightly inferior to BPSK-PRN but will perform better in MC-CDT transmissions.

The difference in cross-correlation values between CDT and FDT/MC-CDT is a serious impediment to the development of a robust CDT-based MBES using the same bandwidth for all sectors. In situations where the backscatter is unknown or varies significantly, a suitable alternative may consist in allocating the same subband to sectors with expected comparable target strength (MC-CDT). As the signal dynamic range varies strongly with the steering angle, CDT separations of sectors received only from comparable steering angle is a more robust solution.

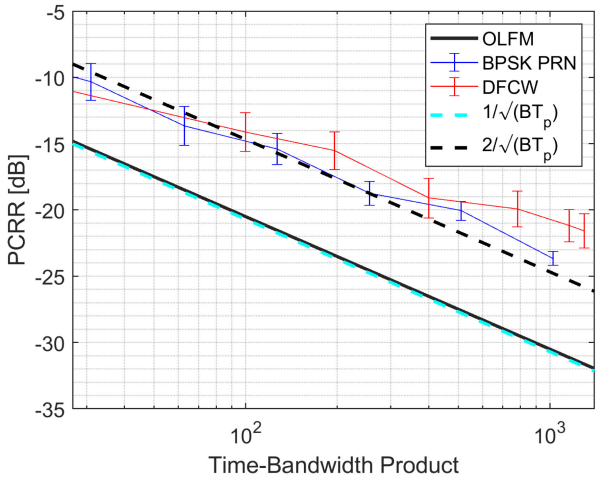

Fig. 7. Mean PCCR versus TBP measured on the set of simulated signals (solid line), the vertical line indicates upper and lower values within the set. The theoretical values are indicated by dashed-lines. A large value for the TBP is required to achieve sufficient orthogonality.

TABLE III
CHARACTERISTICS OF THE SIMULATED MBES SYSTEM (THE ACQUISITION GEOMETRY IS IDENTICAL TO THE ILLUSTRATION IN FIG. 1)

Parameter	Value
Array geometry	Mill's cross [1]
Center frequency (f_0)	300 kHz
System bandwidth (B_{tot})	34 kHz
Nb sectors (across; along)	(3 x 2 swaths)
Along-track resolution (β_{Tx})	1°
Across-track resolution (β_{Rx})	1°
Array tapering (Tx/Rx)	Dolph-Chebyshev: 30 dB [55]
Sector opening angle (β_{sector})	40°
Sector directions across (θ_i)	-30°, 0° and 30°
Swath directions along (ψ_i)	-0.5° and 0.5°
Seafloor	Flat - 100 m
BackScatter mode	Fully dev speckle
Number of realizations	30

IV. Simulated Case Study

We assess the feasibility of orthogonal waveforms for an MBES by simulating a multisector system and a mapping scenario with realistic values in the sonar equation (3). Then, we compare the performance of different orthogonal transmission sequences that are designed based on the waveforms presented in Section III-B4.

A. Simulation Setup

We have simulated a generic MBES system comparable to an EM2040 [51]. It has a center frequency of 300 kHz, a total bandwidth of 34 kHz, and six sectors (two swaths of three sectors, identical to Fig. 1). The characteristics of the sonar are described in Table III.

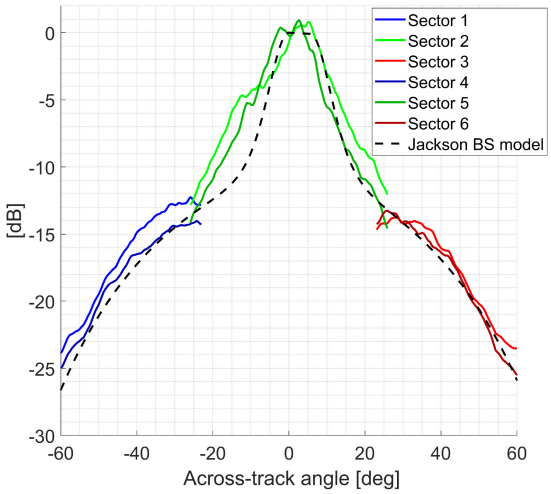

Fig. 8. Simulated BL. This curve is the sum of the BS, the emission sector beam pattern and the transmission losses ($\mathrm{BP}_T(\theta_i, \phi_i) - 2\mathrm{TL}_i + \mathrm{BS}_f(\theta)$). Jackson backscatter model [54] for a medium silt sediment at 300 kHz is shown for reference.

We have used the ultrasound simulator Field II [52], [53] that models the three-dimensional sound field radiated and received by the antenna to generate unprocessed sonar channel data.

We have considered a flat seafloor at 100 m. This depth corresponds to the conventional operating range of a 300-kHz commercial product employing frequency modulation. The seafloor has been modeled as a collection of points with omnidirectional directivity and with uniform random position (x, y) and Gaussian-distributed amplitude. Moreover, the number of points was designed to achieve an average density of 50 points per resolution cell. We have simulated an along track extension of the seafloor of ± 50 m to capture the effects of transmitted sidelobes. We have simulated the seafloor roughness by randomly perturbing the vertical position z of each point. This parameter was adjusted until obtaining an angular backscatter $\mathrm{BS}(\theta)$ with a desired specular reflection effect. Fig. 8 shows the simulated dynamic range of each sector in absence of coding, obtained from (1): $\mathrm{BP}_T(\theta_i, \phi_i) - 2\mathrm{TL}_i + \mathrm{BS}(\theta_i)$. This figure was obtained by simulating independently each sector with the same narrowband CW pulse, at the same frequency band. A medium-silt backscatter model (Jackson, [54]) with transmission loss $2\mathrm{TL}_i$ is plotted for comparison.

The backscattered wavefield is received at each element of the receive antenna. The signal processing part followed the steps described in Fig. 2. After compensating for the transmission delay t_i associated to each pulse s_i, each sector was individually beamformed in a separated angular window and matched filtered with the reference signal. A Dolph–Chebyshev window [55] with a uniform sidelobe level at -30 dB was applied on the transmit and receive arrays, which ensured a realistic [10] and uniform level for the crosstalk of Types II and III. Then, the full swaths were reconstructed by combining three sector images. Uncorrelated additive white Gaussian noise was added on the raw channel data, and the noise power was identical in all simulations. Finally, bottom detection was performed on the signal envelope using the *center-of-gravity* method described in [1] and [56]. In each beam, we have selected a time interval defined by a falloff of 10 dB below the peak value, then computed the mean instant, weighted by the signal amplitude.

B. Transmitted Sequences

We simulated five transmission scenarios where the same system bandwidth B_{tot} is shared differently between sectors. Cases (a) and (b) are conventional frequency-divided transmissions. Cases (c) and (d) are MC-CDT. Finally (e) corresponds to CDT. Table IV summarizes the waveform characteristics and the values of the associated metrics for each scenario. Fig. 9 shows the time–frequency allocation of the transmitted sequences, where colors indicate the spatial location of the six sectors (consistent with Fig. 1).

Each CW pulse was transmitted one by one, enabling the use of a maximum source level (three times higher than the other scenarios), whereas for modulated waveforms, the three sectors of the same swath were emitted at the same time (source level reduced by three). A pulse length of 30 ms was selected in the modulated waveforms. This value provides a large TBP needed for sufficient orthogonality (see Fig. 7) and ensures that the cross-correlated signals are always beam limited. The pulse length was realistic, as 60 ms of total transmission is far below the blind zone limitation. Conventional frequency-divided (a) CW and (b) LFM allocate the largest part of the system bandwidth to frequency guard bands and have the narrowest bandwidth per sector. LFM offers the best cross-correlation properties, whereas CW has minor autocorrelation sidelobes. In the MC-CDT scenarios, (c) employs orthogonal-LFM signals with three frequency bands while (d) employs discrete frequency-coding waveform with two frequency bands. Sectors with the same across-track coordinates were allocated to different frequency bands. The low-interband PCCR values mitigate the crosstalk of Type I, whereas the high-intraband PCCR is sufficient for reducing the other types of crosstalk.

In (e), binary phase modulation with orthogonal sequences is used to share the full system bandwidth between sectors without frequency guard bands. The homogeneous intraband PCCR properties between codes ensure equitable crosstalk suppression between sectors. Due to the reduced performance of the intraband PCCR compared to its interband counterpart, we still expect higher crosstalk residuals on the data. Tapering was applied on all waveforms. A von Hann window [55] is used on the frequency-divided CW pulses. A Tuckey window [55] with parameter 0.2 was used to minimize the resolution loss on other modulated waveforms. Finally, to assess the robustness of the techniques in the presence of significant backscatter contrast varying between sectors along-track (crosstalk Type I), we performed simulations where the source level of the second swath was gradually reduced.

V. Results

In this section, we compare the performance of the simulated transmission schemes at three different levels. 1) First, we evaluate the imaging performance and crosstalk residuals on water-column data and beam time-series. 2) Then, we assess

TABLE IV
CHARACTERISTICS OF THE SIMULATED TRANSMISSION SEQUENCES

					PASR [dB]		PCRR [dB] Intra band		PCRR [dB] Inter band	
	Case	Δf	Δf_{guard}	T_p	max	min	max	min	max	min
FDT: CW 6 band	(a)	6×3.2 kHz	5×3 kHz	320 μs	-	-	-	-	-16,9	-48,9
FDT: LFM 6 bands	(b)	6×3.2 kHz	5×3 kHz	30 ms	-13,4	-13,4	-	-	-100.7	-153.8
MC-CDT: OLFM 3 bands	(c)	3×20 kHz	2×3 kHz	30 ms	-13,3	-13,3	-25,7	-25,8	-94,4	-143.9
MC-CDT: DFCW 2 bands	(d), (f)	2×16 kHz	1×3 kHz	30 ms	-14.8	-17,0	-17,5	-18,0	-52.3	-52.3
CDT: PBSK 1 band	(e), (g)	34 kHz	0 kHz	30 ms	-23,3	-28,3	-23,1	-24,2	-	-

Performance	Minimum	Moderate	Good

the accuracy of the bottom detection for each scenario and for different source levels. 3) Finally, we compare the performance of each method as a function of the additive noise power.

A. *Effect on Water-Column Images*

Fig. 10 shows the processed water-column data for each scenario presented in Fig. 9. The beamformed images correspond to the second swath. The crosstalk (Type I) of the first swath affects the signal and the upper part of the water-column. In all cases with a constant source level, the echo is visible at 100 m.

In the FDT-CW case (a), the signal is clearly visible but the low energy of the transmitted pulse leads to a medium SNR (20 dB) near nadir and about 10 dB at 50°. FDT-LFM (b) achieves the cleanest water-column images with no crosstalk and no visible noise within the dynamic range of the image. This result is explained by the extremely low cross-correlation values of the LFM waveforms between bands and the pulse compression gain.

For the MC-CDT scenarios (c) and (d), the echo from the second swath is well separated from the crosstalk and visible at 100 m. The SNR is high thanks to the pulse-compression gain. Crosstalk artefacts are visible with both transmission schemes. The OLFM scheme offers a clean image with an artefact of low amplitude (-35 dB) in the left part of the central sector. This effect is interpreted as the presence of a strong scatter at the border between sectors 1 and 5, which share the same frequency band. On the other hand, the water-column image appears more noisy with the DFCW scheme (d). This effect is explained by the high autocorrelation sidelobes (maximum PASR at -15 dB). Moreover, a vertical artefact induced by the specular reflection and the autocorrelation sidelobes is visible. The external sectors appear less affected by crosstalk and autocorrelation sidelobes artefacts, as sectors with the same across-track coordinates are allocated in different frequency bands.

Finally in the CDT case (e), the orthogonal properties of the BPSK-PRN waveform have successfully separated the 6 sectors sharing the 34-kHz bandwidth. The echo of the second swath is clearly visible at 100 m as it is for the other transmission schemes. However, crosstalk artefacts caused by the autocorrelation sidelobes and the cross-correlation functions are now visible in the water-column. The CL varies from low to moderate, which is sufficient for bottom detection. Near nadir, the SCR does not exceed 20 dB while it reaches 10 dB at 50° as the power of the backscattered signal decreases in the pulse-limited regime expressed in (2). The amplitude of the crosstalk remains reasonable (inferior to the additive white Gaussian noise of the FDT-CW case), which is sufficient for MBES bathymetry measurement. However, the image is not as clear as case (b). The crosstalk can potentially hinder the presence of a target in the water-column or confuse a human interpreter.

Fig. 10(f) and (g) reproduces Fig. 10(c) and (d) with an increased source level for the first swath (+35 dB and +11 dB, respectively). This scenario corresponds to a strong backscatter contrast between the two swaths (crosstalk Type I). The water-column appears very noisy and it becomes difficult to clearly distinguish the echo of the second swath from the background. This example illustrates the limitation of the MC-CDT and CDT compared to the conventional FDT.

Fig. 11 shows examples of time-series after beamforming in two directions (near and far-across). For normal source level, the signal is clearly visible. For CDT, the CL is smaller than the NL obtained with the conventional FDT-CW but higher than the FDT-LFM. We observe that the crosstalk induced noise and the additive white Gaussian noise have a similar nature. For the increased source level, the echo at 4° is still visible while the beam at 40° is highly affected by the crosstalk.

B. *Bottom Detection Accuracy*

Fig. 12 shows the statistics of the depth estimation error for the two swaths. For each steering angle, we computed the error and extracted the percentile values from a total of

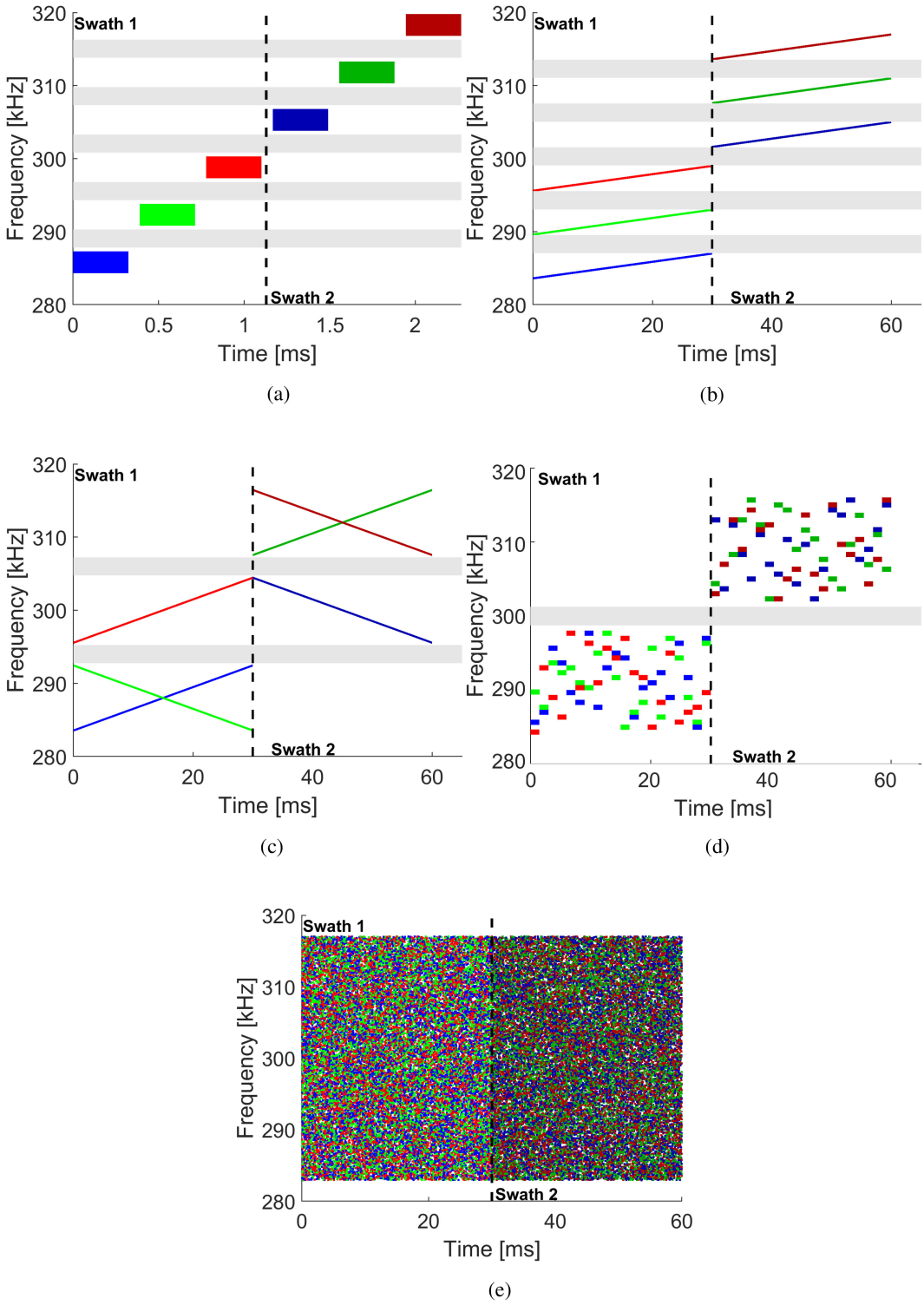

Fig. 9. Time–frequency allocation of the simulated transmissions sequences. (c)–(e) These can be viewed as made from a 2-D representation of Figs. 4–6. Frequency guard bands of 3 kHz are indicated in gray. The color code indicates the location of the six sectors as presented in Fig. 1.

60 independent seabed realizations. Color shades indicate the range of 10 percentiles while the thick black line corresponds to the root-mean-square error. First, all scenarios with normal source level lead to correct bottom detection (root-mean-square error within the range of the center of gravity detector accuracy specified in [56]).

The FDT-CW case displays an increased error after 50° due to low SNR (10 dB). Thanks to pulse compression, this problem does not affect the other transmission schemes. The best performance is obtained with the OLFM transmission. This technique combines the benefits of both a good resolution and the LFM autocorrelation function. The MC-CDT DFCW offers also

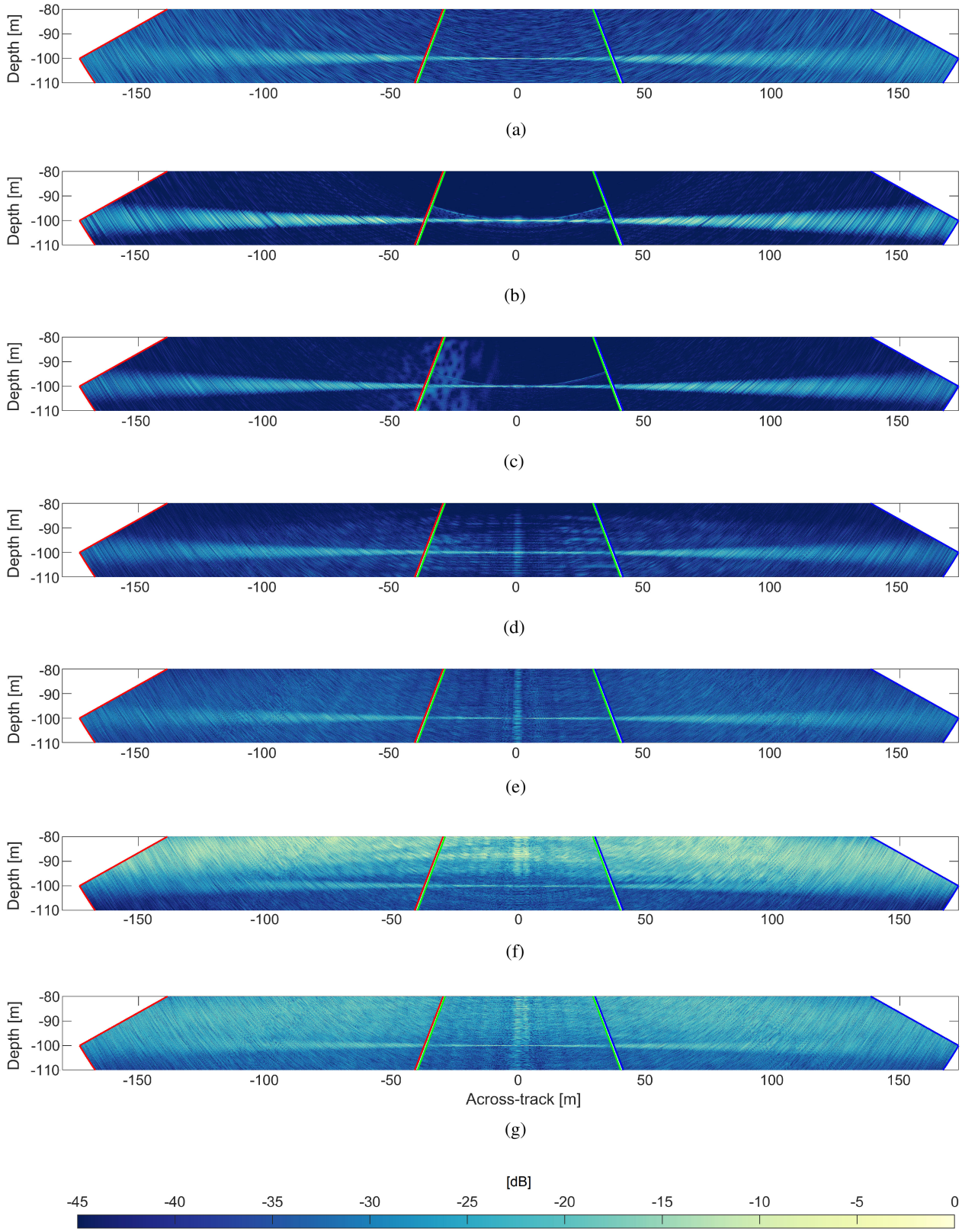

Fig. 10. Simulated water-column data of the different encoding schemes presented in Table IV and Fig. 9. The color frames indicate the sector number. The beamformed images correspond to the second swath. The crosstalk (Type I) of the first swath affects the signal and the upper part of the water column. (a) FDT: CW 6 bands (normal source level). (b) FDT: LFM 6 bands (normal source level). (c) MC-CDT: OLFM 3 bands (normal source level). (d) MC-CDT: DFCW 2 bands (normal source level). (e) CDT: BPSK-PRN 1 band (normal source level). (f) MC-CDT: DFCW 2 bands (source level of the cross talk: $+35$ dB). (g) CDT: BPSK-PRN 1 band (source level of the cross talk: $+11$ dB).

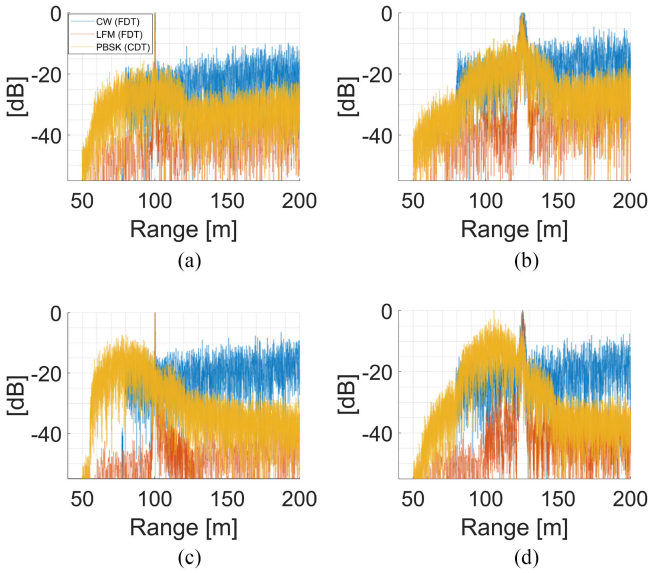

Fig. 11. Example of beam time-series for two steering angles. (a) and (b) Normal source level. (c) and (d) Increased source level of the crosstalk (SL:+11 dB). For a normal source level, the multiplicative noise of the BPSK-PRN case is inferior to the additive white Gaussian noise of the CW-FDT. (a) Beam at 4° (normal SL). (b) Beam at 4° (increased SL). (c) Beam at 40° (normal SL). (d) Beam at 40° (increased SL).

good accuracy in spite of the autocorrelation sidelobes. Finally, with the CDT, the six sectors are accurately detected in the $\pm$ 50° window (inferior to 0.4%). Beyond 50°, the SCR becomes low and the bottom detection accuracy is reduced (0.5%). This example confirms that the new proposed transmission schemes are able to share the system bandwidth between sectors while maintaining bottom detection performance.

Fig. 12(f) and (g) shows the detection accuracy of cases (c) and (e) with an increased source level for the first swath producing crosstalk. This example illustrates the limit of the proposed MC-CDT and CDT methods in the presence of rapid changes in the sediment backscatter value. In these two scenarios, the signal has been completely jammed by the crosstalk, leading to false detections. We note that the boundaries between sectors are particularly affected as they share the same frequency band and have a similar BL. Fig. 13 shows the root-mean-square error obtained in the beam at 40° (second swath, sector 6) versus the difference in source level between the two swaths. The CDT is the least robust as the error increases beyond 10 dB of additional source level. The MC-CDT has good performance until 32 and 39 dB of an additional source level. This value is consistent with the expected level of the second and third types of crosstalk.

C. Signal-to-Noise Ratio

Fig. 14 shows the effect of the NL on the root-mean-square error. We repeated the simulation while increasing the magnitude of the additive white Gaussian noise added to raw channel data and assessed the accuracy around the beam steered at 40° for each scenario. This result illustrates a minor drawback of using a large bandwidth.

At low noise power (>-10 dB), the root-mean-square error of the full swath clusters near 0.2%, which indicates a comparable level of accuracy between scenarios. The CW scenario (a) is the most affected, whereas the conventional LFM (c) can handle the highest noise power. We note the difference of 20 dB, consistent with the pulse compression gain BT_p.

The proposed (b), (c) MC-CDT and (e) CDT techniques are situated between these two extreme cases. Moreover, the maximum input SNR tolerable appears to be correlated with the waveform bandwidths order. We interpret this result as a consequence of a reduced cell footprint in the pulse-limited regime as expressed in (2).

VI. Discussion

In the current study, we have considered the possibility of employing coded waveforms as an alternative to frequency division for multisector MBES bathymetry. First, our analytical model in Section II provided guidelines for managing the crosstalk budget. For a given sonar system and expected seafloor properties, the model can be used to design transmission sequences with CDT and MC-CDT fitting these budgets. The techniques were tested with a generic MBES configuration and the seabed backscatter was comparable to a sediment with a significant backscatter dynamic range. We have limited the scope of the study to amplitude detection, future studies may consider the effect of crosstalk on other estimators, such as the phase difference bottom detector. For the same total bandwidth and transmission time, the obtained results demonstrated the possibility to share bandwidth between sectors while maintaining bottom detection performance (see Fig. 12). Also further work may test more realistic noise models. Compared to FDT, the bandwidth of each sector was considerably increased (by a factor of nearly 11 for CDT and between 3 and 5 for MC-CDT). Table V summarizes the benefits and setbacks discussed in this section.

The benefits gained compared to traditional transmissions include the following: First, sectors sharing the same spectral support will lead to a strong mitigation of the frequency bias affecting sediment acoustic characterization performance and the radiometric correction described in [4] and [8]. Second, a net gain of bandwidth per sector. This improves the range resolution and offers a better way to characterize the frequency response of the sediments. The improvement in range resolution can also be traded against speckle reduction through frequency compounding processing [57], [58]. Third, a more efficient usage of the system bandwidth since it removes frequency guard bands. We demonstrated that CDT enables wideband multisector signals for the time-bandwidth cost of a narrowband multisector FDT MBES. Fourth, the maximum number of sectors can also be increased thanks to the diversity of codes.

The main setback, compared to conventional transmissions, is the system robustness. As we showed in Figs. 7 and 13, orthogonal waveform provides a power of separation inferior to FDT. This can penalize CDT systems in environments where the acoustic dynamic range is important. Therefore, careful system design that integrates *a priori* knowledge on the environment is recommended. In addition, the conclusion of this study may not

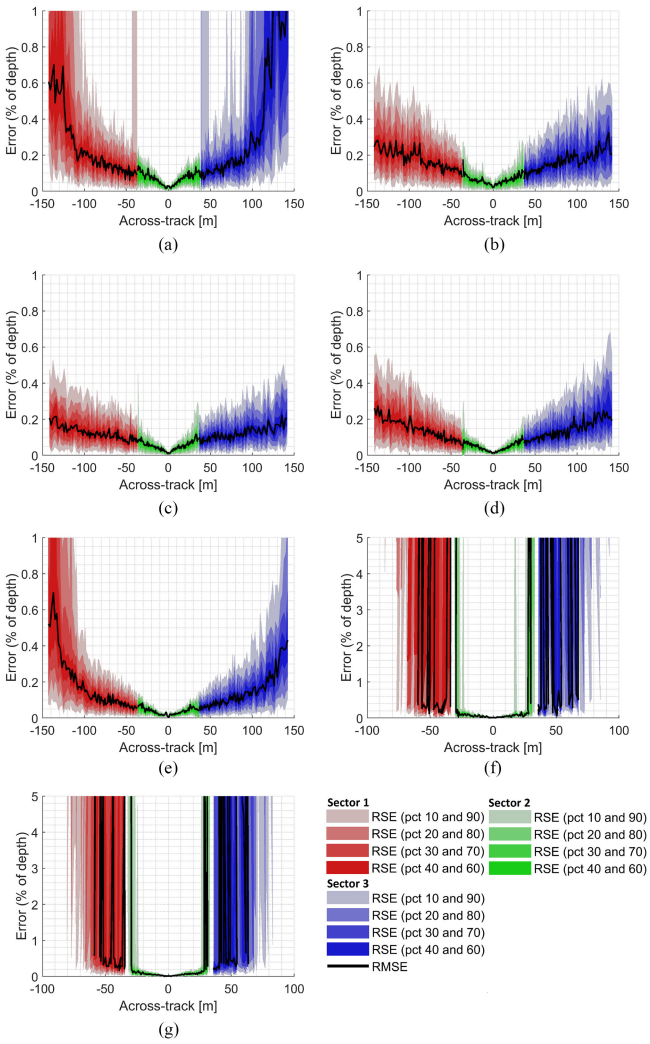

Fig. 12. Statistics of the bottom detection accuracy obtained on the different scenarios for 30 seabed realizations. The color code indicates the location of the sectors as presented in Fig. 1. (a) FDT: CW 6 bands (swath 1 and 2). (b) FDT: LFM 6 bands (swath 1 and 2). (c) MC-CDT: OLFM 3 bands (swath 1 and 2). (d) MC-CDT: DFCW 2 bands (swath 1 and 2). (e) CDT: BPSK-PRN 1 band (swath 1 and 2). (f) MC-CDT: DFCW 2 bands (Source level of the crosstalk: +35 dB), (swath 2 only). (g) CDT: BPSK-PRN 1 band (Source level of the crosstalk: +11 dB), (swath 2 only).

be generalized to all MBES systems and survey configurations. In Sections VI-A–VI-D, we discuss the tradeoff and potential limitations of the methods.

A. *Time-Bandwidth Budget*

Effective code division requires waveforms with a large TBP, as illustrated in Fig. 7. It must be noted that the highest values may not be achieved by all systems available today. However, considering that modern systems can offer a wide operating bandwidth, we have suggested values that are not unrealistic.

Depending on the survey configuration, it may be advantageous to favor the use of either bandwidth or the pulse length. On the one hand, increasing the pulse length will provide a net gain of SNR in the presence of additive white Gaussian noise. However, as the length of the pulse increases, the likelihood of receiving more sectors simultaneously will also increase [see the model in (10)], which may raise the CL. This strategy is preferred in deep water operations where the SNR is usually low, but the water depth allows the transmission of long signals. On the other hand, increasing bandwidth increases the noise power, which translates into a loss in SNR. Wideband pulses will lead to a moderate reduction of the maximum range, as shown in Fig. 14 , which is still much better than with a CW system. The effect of bandwidth on the SCR is more balanced. In spite of the advantages mentioned earlier in this discussion, increasing the bandwidth may not always be beneficial for bathymetry accuracy as it reduces the signal power per resolution cell. However, a short pulse length enables easier time separation of the sectors, which reduces the multiplicative noise previously mentioned. This is a suitable option for shallow water where the water depth prevents the transmission of long sequences and the SNR is usually high. Finally, further study may compare the effects of these two parameters on the total SNR.

B. *Residual Crosstalk*

Contrary to frequency-divided MBES, the cross correlation of orthogonal signals induces artefacts ranging from 35 dB to a maximum of 10 dB of SCR [visible in Fig. 10(c)-(e)]. Although

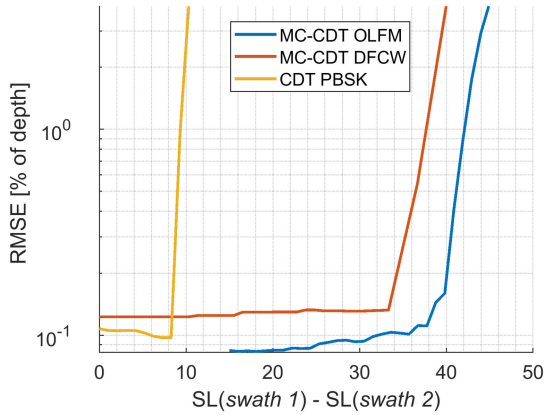

Fig. 13. Effect of increasing the source level of the first swath (Crosstalk type I) on the accuracy of the beam at 40°. The SNR is measured on raw channel data before processing.

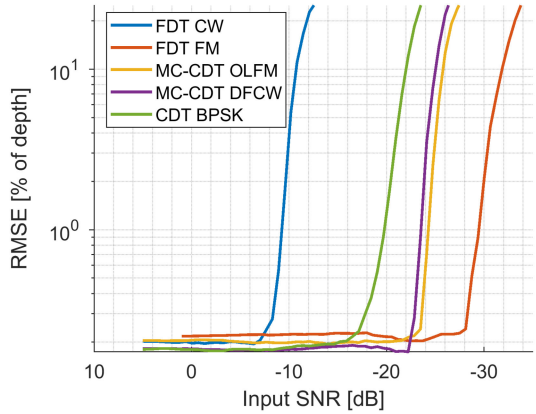

Fig. 14. Effect of the input SNR on the bottom detection accuracy (root-mean-square error). The SNR is measured on raw channel data before processing.

the low magnitude of the artefacts does not affect significantly the bottom detection accuracy, they may be confused by a human interpreter with targets like a school of fish or a gas plume in the water-column. Small targets in the water-column may be particularly vulnerable to this noise. Strong target strength may also contaminate the water-column data as in the simulated scenario with a modified source level showed in Fig. 10(c)–(e). Moreover, the autocorrelation sidelobes of BPSK-PRN/DFCW may also mask a small target located close to the seafloor. This effect will be more pronounced in shallow water, where the sidelobes occupy a larger fraction of the water depth. Future studies will compare the use of mismatched filters obtained by correlating a longer reference signal to lower the PASR [41, Ch. 4.10.3] and [23].

Also, as the orthogonal sequences used for modulating the signals can be computed in advance, it may be advantageous to improve the orthogonality performance by searching for the best subset of codes with numerical optimization algorithms [26], [42]. These techniques may benefit from the SCR models presented in Section II for constraining the search to some given specifications.

TABLE V
SUMMARY OF OBSERVED POTENTIAL BENEFITS AND SETBACKS CONCERNING THE SUGGESTED TECHNIQUES

	Performance vs FDT		
	MC-CDT		**CDT**
MBES property	**OLFM**	**DFCW**	**BPSK-PRN**
Range resolution	increased		Highly Increased
Maximum No. sectors	Two per band	-Unlimited No. codes -Limited by the cross-talk	
Mapping accuracy	Similar		
Water-column	Similar	Induces multiplicative noise-like cross-talk	
Maximum range	-Inferior to narrowband LFM -Much better than CW		
Robustness to backscatter contrast	Good between bands		Limited
MBES processing	**OLFM**	**DFCW**	**BPSK-PRN**
Radiometric correction	Same per band		Same for all sectors
Backscatter	Bias only per band		No frequency bias
Processing cost	Identical	Doppler correction requiered	
Phase detection accuracy	Further study requiered		
Effect	**Setback**	**Neutral**	**Improvement**

To complete the study of orthogonal waveforms for the MBES application, a feasibility study for the phase bottom detection must also be made. We have omitted this in our study to limit the scope of the work and maintain clarity.

C. *Waveform Transmission Considerations*

For active sonar transducers, BPSK-PRN signals may be difficult to transmit. The instantaneous phase transitions cause extended spectral sidelobes. The piezo-ceramic transducers may not handle properly those phase transitions and the waveforms might be distorted [59].

For wideband signals, it could be advantageous to use waveforms with continuous phase between bits. Costas frequency hopping, originally developed for active sonar applications, belongs to this class [22], [47]. Minimum shift keying is also used for implementing binary codes [43] with continuous phase. A practical implementation of such a BPSK-PRN waveform is suggested in [15, p. 145]. This consists in slowing the phase-switching rate of the transmitted signal to reduce its spectrum tail.

This article simulated the impulse response of the sonar system as a bandpass filter over the 200–400 kHz band. The transmitted waveforms have been bandpass filtered after the first spectral sidelobes. This operation did not significantly affect the autocorrelation and cross-correlation properties. However, more

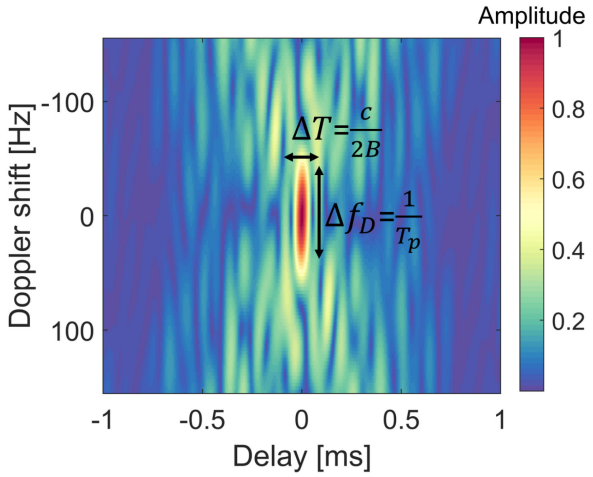

Fig. 15. Ambiguity function of the Costas frequency coded pulse shown in Fig. 6. (ΔT: time resolution, Δf_D: Doppler resolution). The Doppler mismatch cannot be ignored beyond $f_D T_P < 1/4$.

aggressive bandpass filtering inside the spectral main-lobe will likely impact the performance [15], [43].

D. Doppler Sensitivity and Correction

This article has not considered the effect of Doppler shifts caused by the ship motion. Contrary to conventional CW systems, orthogonal spread spectrum waveforms are very sensitive to Doppler shifts. This sensitivity can be explained by the "thumbtack" shape of its ambiguity function (see Fig. 15), which consists of a central lobe, narrow in range and Doppler. The pseudorandom modulations that provide the orthogonal properties are responsible of this effect. The effect is more important that a simple time shift of the mainlobe observed with LFM MBES [5], [60], [61] and a Doppler mismatch f_D caused by a platform velocity V can potentially shrink the signal peak and reduce the SCR. According to the explainations in [41, Ch. 4.10.1], the matched filter loss is less than 1 dB f_D if

$$f_D T_P < \frac{1}{4} \Leftrightarrow V < \frac{c}{4 T_p f_0}. \tag{18}$$

A possible solution consists in updating the matched filters with a Doppler corrected version of the pulse. For typical pulses used in this article ($T_p = 30$ ms, $f_0 = 300$ kHz), we obtain a maximum tolerable velocity of $V = 0.047$ m/s, which is five times the accuracy of a modern inertial measurement unit (0.01 m/s) [62], [63]. Therefore, a Doppler corrected matched filter appears to be a suitable solution. For deep waters, where low-frequency systems employ very long pulses, more advanced solutions must be considered. For instance up–down Doppler robust hyperbolic frequency modulation [64] can be a potential solution.

VII. Conclusion

We have studied the possibility to use orthogonal waveforms for allocating the same frequency band to multiple sectors in MBES mapping operations.

First, this article provides an analytical model describing the power and crosstalk budgets of any multisector MBES and seafloor type. The model can be used to design transmission sequences fitting these budgets. Specific waveforms with different properties are reviewed and compared. We show that waveforms employing CDTs can achieve a separation of 10–25 dB between signal and crosstalk. Compared to conventional FDT, the proposed designs offer a considerably better range resolution, and highly reduce the frequency bias affecting different sectors. A hybrid transmission method, combining both waveform orthogonality and frequency division is suggested as a way to increase the system robustness in hostile survey conditions.

We assessed the feasibility of these techniques for MBES imaging and mapping through a simulated case study. The simulations reproduced the radiated sound-field of a multisector sonar and emulated a BS with a specular reflection effect. For the same total time-bandwidth budget, we simulated FDT, CDT, and MC-CDT multisector transmissions schemes and compared their performance on bottom detection based on signal amplitude. The results demonstrate the possibility of sharing the bandwidth between sectors while maintaining the bottom detection performance. However, CDT displayed low-magnitude crosstalk artefacts inherent to the matched filter residuals. Such artefacts may potentially hinder the interpretation of water-column images by an operator. In addition, we show that the maximum range of a CDT system is moderately reduced compared to the conventional FDT. MC-CDT can offer a satisfactory solution to these two problems.

To conclude, the proposed techniques may provide new modes to the current or next generation of MBES systems. The main challenges are associated to the management of the crosstalk budget, which can be a limitation in some applications. The mode should more be viewed as a complement to conventional FDT. We recommend careful waveform and transmission sequence design to fit the mission requirements.

Acknowledgment

The authors would like to thank Darrell Jackson from Applied Physics Laboratory, University of Washington, Seattle, WA, USA, for providing code to produce the sediment backscatter model used for comparison in Fig. 8. The authors also would like to thank Anthony Lyons from the Center for Coastal and Ocean Mapping / Joint Hydrographic Center, University of New Hampshire, Durham, NH, USA, for valuable discussions on seabed backscatter. The authors also thank the three anonymous reviewers for their comments and suggestions that have improved the quality of this work.

References

[1] X. Lurton, *An Introduction to Underwater Acoustics: Principles and Applications*, 2nd ed. London, U.K.: Springer-Verlag, 2010.
[2] J. E. H. Clarke, "Multibeam echosounders," in *Submarine Geomorphology*. Berlin, Germany: Springer-Verlag, 2018, pp. 25–41.
[3] V. Renard and J.-P. Allenou, "Sea beam, multi-beam echo-sounding in Jean Charcot"—Description, evaluation and first results," *Int. Hydrographic Rev.*, vol. 56, no. 1, 1979.

[4] A. C. G. Schimel *et al.*, "Multibeam sonar backscatter data processing," *Mar. Geophys. Res.*, vol. 39, no. 1, pp. 121–137, Jun. 2018, doi: 10.1007/s11001-018-9341-z.

[5] J. E. H. Clarke, "The impact of acoustic imaging geometry on the fidelity of seabed bathymetric models," *Geosciences*, vol. 8, no. 4, 2018, Art. no. 109.

[6] Kongsberg, "SIMRAD ME70 datasheet," 2020. [Online]. Available: https://www.kongsberg.com/maritime/products/mapping-systems/fishery-research/scientific-multibeam-systems/simrad-me70/.

[7] X. Lurton, "Backscatter measurements by seafloor-mapping sonars: Guidelines and recommendations," *GeoHab Backscatter Working Group*, pp. 1–200, 2015.

[8] A. D. Hiroji, "Extracting sonar relative beam patterns for multisector multibeam sonar," Ph.D. dissertation, Dept. Geodesy Geomatics Eng., Univ. New Brunswick, Fredericton, NB, Canada, 2016. [Online]. Available: http://www2.unb.ca/gge/Pubs/TR304.pdf

[9] M. A. Ainslie, *Principles of Sonar Performance Modelling*. Berlin, Germany: Springer, 2010.

[10] X. Lurton, "Modelling of the sound field radiated by multibeam echosounders for acoustical impact assessment," *Appl. Acoust.*, vol. 101, pp. 201–221, 2016.

[11] Kongsberg, "EM 712 datasheet," May 2019. [Online]. Available: https://www.kongsberg.com/maritime/products/mapping-systems/multibeam-echo-sounders/em-712-multibeam-echosounder-max.-3600-m/

[12] Kongsberg, "*E*M 304 datasheet," May 2019. [Online]. Available: https://www.kongsberg.com/maritime/products/mapping-systems/multibeam-echo-sounders/em-304-multibeam-echosounder-max.-8000-m?OpenDocument

[13] A. J. Viterbi, *CDMA: Principles of Spread Spectrum Communication*. Reading, MA, USA: Addison-Wesley, 1995.

[14] W. Wang, "Mitigating range ambiguities in high-PRF SAR with OFDM waveform diversity," *IEEE Geosci. Remote Sens. Lett.*, vol. 10, no. 1, pp. 101–105, Jan. 2013.

[15] N. Levanon and E. Mozeson, *Radar Signals*. Hoboken, NJ, USA: Wiley, 2004.

[16] C. Cook, *Radar Signals: An Introduction to Theory and Application*. New York, NY, USA: Elsevier, 2012.

[17] G. Galati, G. Pavan, and A. De Franco, "Orthogonal waveforms for multistatic and multifunction radar," in *Proc. 9th Eur. Radar Conf.*, Oct. 2012, pp. 310–313.

[18] H. Deng, "Polyphase code design for orthogonal netted radar systems," *IEEE Trans. Signal Process.*, vol. 52, no. 11, pp. 3126–3135, Nov. 2004.

[19] S. Harman, "Orthogonal polyphase code sets with master codes," in *Proc. Int. Waveform Diversity Des. Conf.*, 2004, pp. 1–5.

[20] C. J. Nunn and L. R. Welch, "Multi-parameter local optimization for the design of superior matched filter polyphase pulse compression codes," in *Proc. Rec. IEEE Int. Radar Conf.*, 2000, pp. 435–440.

[21] K. J. Gartz, "Generation of uniform amplitude complex code sets with low correlation sidelobes," *IEEE Trans. Signal Process.*, vol. 40, no. 2, pp. 343–351, Feb. 1992.

[22] S. P. Pecknold, W. M. Renaud, D. R. McGaughey, J. A. Theriault, and R. F. Marsden, "Improved active sonar performance using Costas waveforms," *IEEE J. Ocean. Eng.*, vol. 34, no. 4, pp. 559–574, Oct. 2009.

[23] M. S. Rashed, M. Meijer, and P. D. Teal, "Mismatched filtering of Doppler tolerant codes for multi-code sonar systems," in *Proc. MTS/IEEE OCEANS Conf.*, Seattle, WA, USA, Oct. 2019, pp. 1–10.

[24] T. Dean, "The use of pseudorandom sweeps for vibroseis surveys," *Geophysical Prospecting*, vol. 62, no. 1, pp. 50–74, 2014.

[25] M. B. Mueller, D. F. Halliday, D.-J. van Manen, and J. O. A. Robertsson, "The benefit of encoded source sequences for simultaneous source separation," *Geophysics*, vol. 80, no. 5, pp. V 133–V143, 2015.

[26] M. B. Mueller, D. F. Halliday, D.-J. van Manen, and J. O. A. Robertsson, "Optimizing near-orthogonal air-gun firing sequences for marine simultaneous source separation," *Geophysics*, vol. 81, no. 6, pp. V 415–V423, 2016.

[27] H. Nasreddin, T. Dean, and K. Iranpour, "The use of pseudorandom sweeps to reduce interference noise in simultaneous vibroseis surveys," *ASEG Extended Abstr.*, vol. 2012, no. 1, pp. 1–4, 2012.

[28] J. Sallas, J. Gibson, P. Maxwell, and F. Lin, "Pseudorandom sweeps for simultaneous sourcing and low-frequency generation," *Leading Edge*, vol. 30, no. 10, pp. 1162–1172, 2011.

[29] G. Krieger, "MIMO-SAR: Opportunities and pitfalls," *IEEE Trans. Geosci. Remote Sens.*, vol. 52, no. 5, pp. 2628–2645, May 2014.

[30] C. Diego, A. Hernández, A. Jiménez, F. J. Álvarez, R. Sanz, and J. Aparicio, "Ultrasonic array for obstacle detection based on CDMA with Kasami codes," *Sensors*, vol. 11, no. 12, pp. 11 464–11475, 2011.

[31] F. Gran and J. A. Jensen, "Spatial encoding using a code division technique for fast ultrasound imaging," *IEEE Trans. Ultrason., Ferroelect., Freq. Control*, vol. 55, no. 1, pp. 12–23, Jan. 2008.

[32] T. Misaridis, "Ultrasound imaging using coded signals," Ph.D. dissertation, Dept. Elect. Eng., Tech. Univ. Denmark, Lyngby, Denmark, 2001.

[33] T. Misaridis and J. A. Jensen, "Use of modulated excitation signals in medical ultrasound. Part I: Basic concepts and expected benefits," *IEEE Trans. Ultrason., Ferroelect., Freq. Control*, vol. 52, no. 2, pp. 177–191, Feb. 2005.

[34] T. Misaridis and J. A. Jensen, "Use of modulated excitation signals in medical ultrasound. Part II: Design and performance for medical imaging applications," *IEEE Trans. Ultrason., Ferroelect., Freq. Control*, vol. 52, no. 2, pp. 192–207, Feb. 2005.

[35] T. Misaridis and J. A. Jensen, "Use of modulated excitation signals in medical ultrasound. Part III: High frame rate imaging," *IEEE Trans. Ultrason., Ferroelect., Freq. Control*, vol. 52, no. 2, pp. 208–219, Feb. 2005.

[36] R. Y. Chiao and X. Hao, "Coded excitation for diagnostic ultrasound: A system developer's perspective," *IEEE Trans. Ultrason., Ferroelect., Freq. Control*, vol. 52, no. 2, pp. 160–170, Feb. 2005.

[37] L. R. Welch and M. D. Fox, "Practical spread spectrum pulse compression for ultrasonic tissue imaging," *IEEE Trans. Ultrason., Ferroelect., Freq. Control*, vol. 45, no. 2, pp. 349–355, Mar. 1998.

[38] M. O'Donnell, "Coded excitation system for improving the penetration of real-time phased-array imaging systems," *IEEE Trans. Ultrason., Ferroelect., Freq. Control*, vol. 39, no. 3, pp. 341–351, May 1992.

[39] B. B. Lee and E. Furgason, "Pseudo-random codes for single-mode and simultaneous multi-mode operation in ultrasonic imaging systems," Tech. Rep. TR-EE 8510, School Elect. Eng., Purdue Univ., West Lafayette, IN, USA, 1985.

[40] R. J. Urick, *Principles of Underwater Sound*, 3rd ed. Los Altos, CA, USA: Peninsula, 1983.

[41] M. A. Richards, *Fundamentals of Radar Signal Processing*. New York, NY, USA: McGraw-Hill, 2005.

[42] B. M. Keel, J. M. Baden, and T. H. Heath, "A comprehensive review of quasi-orthogonal waveforms," in *Proc. IEEE Radar Conf.*, 2007, pp. 122–127.

[43] S. D. Blunt and E. L. Mokole, "Overview of radar waveform diversity," *IEEE Aerosp. Electron. Syst. Mag.*, vol. 31, no. 11, pp. 2–42, Nov. 2016.

[44] P. Vincent, F. Maussang, X. Lurton, C. Sintes, and R. Garello, "Bathymetry degradation causes for frequency modulated multibeam echo sounders," in *Proc. MTS/IEEE OCEANS Conf.*, Oct. 2012, pp. 1–5.

[45] T. Kasami, "Weight distribution formula for some class of cyclic codes," *Coordinated Sci. Lab., Univ. Illinois, Urabana-Champaign, Tech. Rep. R-285*, 1966.

[46] D. V. Sarwate and M. B. Pursley, "Crosscorrelation properties of pseudorandom and related sequences," *Proc. IEEE*, vol. 68, no. 5, pp. 593–619, May 1980.

[47] J. P. Costas, "A study of a class of detection waveforms having nearly ideal range-Doppler ambiguity properties," *Proc. IEEE*, vol. 72, no. 8, pp. 996–1009, Aug. 1984.

[48] J. K. Beard, "Costas arrays and enumeration to order 1030," 2017. [Online]. Available: https://ieee-dataport.org/open-access/costas-arrays-and-enumeration-order-1030

[49] N. Levanon and E. Mozeson, "Modified Costas signal," *IEEE Trans. Aerosp. Electron. Syst.*, vol. 40, no. 3, pp. 946–953, Jul. 2004.

[50] N. Touati, C. Tatkeu, T. Chonavel, and A. Rivenq, "Design and performances evaluation of new Costas-based radar waveforms with pulse coding diversity," *IET Radar, Sonar, Navigat.*, vol. 10, no. 5, pp. 877–891, 2016.

[51] Kongsberg, "EM2040 MK II datasheet," Aug. 2019. [Online]. Available: https://www.kongsberg.com/maritime/products/mapping-systems/mapping-systems/multibeam-echo-sounders/em-2040-multibeam-echosounder-max.-600-m/

[52] J. A. Jensen, "Field: A program for simulating ultrasound systems," in *Proc. 10th Nordicbaltic Conf. Biomed. Imag.*, vol. 4, Suppl. 1, pt. 1: 351–353, 1996.

[53] J. A. Jensen and N. B. Svendsen, "Calculation of pressure fields from arbitrarily shaped, apodized, and excited ultrasound transducers," *IEEE Trans. Ultrason., Ferroelect., Freq. Control*, vol. 39, no. 2, pp. 262–267, Mar. 1992.

[54] M. D. Richardson and D. R. Jackson, "The seafloor," in *Applied Underwater Acoustics*, L. Bjørnø, T. Neigbors, and D. Bradley, Eds. Amsterdam, The Netherlands: Elsevier, Feb. 2017, ch. 8, pp. 469–552.
[55] F. J. Harris, "On the use of windows for harmonic analysis with the discrete Fourier transform," *Proc. IEEE*, vol. 66, no. 1, pp. 51–83, Jan. 1978.
[56] X. Lurton and J.-M. Augustin, "A measurement quality factor for swath bathymetry sounders," *IEEE J. Ocean. Eng.*, vol. 35, no. 4, pp. 852–862, Oct. 2010.
[57] P. A. Magnin, O. T. von Ramm, and F. L. Thurstone, "Frequency compounding for speckle contrast reduction in phased array images," *Ultrason. Imag.*, vol. 4, no. 3, pp. 267–281, 1982.
[58] G. Traney, J. Allison, S. Smith, and O. von Ramm, "A quantitative approach to speckle reduction via frequency compounding," *Ultrason. Imag.*, vol. 8, no. 3, pp. 151–164, 1986.
[59] Y. Pailhas and Y. Petillot, "Wideband CDMA waveforms for large MIMO sonar systems," in *Proc. Sensor Signal Process. Defence*, Sep. 2015, pp. 1–4.
[60] T. H. Mohammadloo, M. Snellen, and D. G. Simons, "An uncertainty assessment of the effect of using FM pulses on MBES depth measurements," in *Proc. 4th Underwater Acoust. Conf. Exhib.*, 2017, pp. 1043–1048.
[61] P. Vincent, C. Sintes, F. Maussang, X. Lurton, and R. Garello, "Doppler effect on bathymetry using frequency modulated multibeam echo sounders," in *Proc. OCEAN Conf.*, Jun. 2011, pp. 1–5.
[62] Kongsberg-Seatex, "MRU5 datasheet," May 2019. [Online]. Available: https://www.kongsberg.com/globalassets/maritime/km-products/product-documents/mru-5-mk-ii---the-ultimate-marine-motion-sensor/Download
[63] Teledyne, "MRU DMS-05 datasheet," May 2019. [Online]. Available: http://www.teledynemarine.com/dms-05
[64] M. Vespe, G. Jones, and C. J. Baker, "Lessons for radar," *IEEE Signal Process. Mag.*, vol. 26, no. 1, pp. 65–75, Jan. 2009.

Antoine Blachet was born in Dijon, France, in 1992. He received the M.S. degree in applied geophysics from the Ecole and Observatoire des Sciences de la Terre (EOST), Strasbourg, France, in 2016, and the Ph.D. degree in signal processing from the University of Oslo, Oslo, Norway, in 2021.

Since 2020, he has been an R&D Engineer in sonar signal processing with Thales Defence Mission Systems. In 2016, he worked for 6 months in the R&D Division, PGS, Oslo, where he studied the impact of air-gun array motions on time-lapse seismic data for monitoring the production of deep geological reservoirs. In 2015, he was also with Sintef, Trondheim, where he tested seismic processing algorithms for sediment classifications based on angular dependence. His research interests include underwater acoustics and signal processing for various applications, including sonar, seismic, and radar.

Mr. Blachet has been a member of SEG and EAGE since 2013.

Andreas Austeng (Senior Member, IEEE) received the M.S. degree in physics and the Ph.D. degree in computer science from the University of Oslo, Oslo, Norway, in 1996 and in 2001, respectively.

Since 2001, he has been a Postdoctoral Research Fellow and an Associate Professor with the Department of Informatics, University of Oslo. He is currently a Professor with the Digital Signal Processing and Image Analysis Group, University of Oslo. His research interests include signal processing for acoustical imaging and algorithms that aim to improve the quality of information extracted from images.

Joaquín Aparicio (Member, IEEE) received the Licentiate degree in physics from the University of Extremadura, Badajoz, Spain, in 2008, and the Ph.D. degree from the University of Alcalá, Henares, Spain, in 2014.

From 2015 to 2018, he was a Postdoctoral Researcher with the Japan Agency for Marine-Earth Science and Technology, Yokosuka, Japan. Since 2018, he has been a Postdoctoral Fellow with the Department of Informatics, University of Oslo, Oslo, Norway. His research interests include acoustic positioning systems, underwater acoustic propagation and communication systems, and signal processing.

Alan J. Hunter (Senior Member, IEEE) received the B.E. (Hons.) and Ph.D. degrees in electrical and electronic engineering from the University of Canterbury, Christchurch, New Zealand, in 2001 and 2006, respectively.

From 2007 to 2010, he was a Research Associate with the University of Bristol, Bristol, U.K., and from 2010 to 2014, he was a Defense Scientist with TNO (Netherlands Organisation for Applied Scientific Research), The Hague, The Netherlands. In 2014, he joined the Faculty of Engineering, University of Bath, Bath, U.K., where he is currently a Senior Lecturer. Since 2017, he has been an Adjunct Associate Professor with the Department of Informatics, University of Oslo, Oslo, Norway. His research interests include underwater acoustics, sonar imaging of the seafloor, and autonomous underwater systems.

Dr. Hunter is an Associate Editor for IEEE JOURNAL OF OCEANIC ENGINEERING.

Roy Edgar Hansen (Senior Member, IEEE) received the M.Sc. and Ph.D. degrees in physics from the University of Tromsø, Tromsø, Norway, in 1992 and 1999, respectively. His Ph.D. dissertation was titled "Measurements in the Mixed Layer by a Bistatic Multi-CW Doppler Sonar."

From 1992 to 2000, he was with the Norwegian research company TRIAD, working on multistatic sonar, multistatic radar, SAR, and underwater communications. Since 2000, he has been with the Norwegian Defence Research Establishment (FFI), Kjeller, Norway, in the field of synthetic aperture sonar. He is currently a Principal Scientist with FFI. He is also an Adjunct Professor in acoustic imaging with the Department of Informatics, University of Oslo, Oslo, Norway. His research interests include synthetic aperture sonar and radar, ultrasound imaging, sonar signal processing, and array signal processing.